Acta Materialia 118 (2016) 140–151

Contents lists available at ScienceDirect

Acta Materialia

journal homepage: www.elsevier.com/locate/actamat

Full length article

A crystal plasticity model for twinning- and transformation-induced plasticity

Su Leen Wong [a, *], Manjunatha Madivala [b], Ulrich Prahl [b], Franz Roters [a], Dierk Raabe [a]

[a] Max-Planck-Institut für Eisenforschung GmbH, Max-Planck-Straße 1, 40237 Düsseldorf, Germany
[b] Institut für Eisenhüttenkunde (IEHK), RWTH Aachen University, Aachen, Germany

ARTICLE INFO

Article history:
Received 18 May 2016
Received in revised form
14 July 2016
Accepted 19 July 2016

Keywords:
Crystal plasticity
Constitutive modeling
Deformation twinning
Martensitic phase transformation

ABSTRACT

A dislocation density-based crystal plasticity model incorporating both transformation-induced plasticity (TRIP) and twinning-induced plasticity (TWIP) is presented. The approach is a physically-based model which reflects microstructure investigations of ε-martensite, twins and dislocation structures in high manganese steels. Validation of the model was conducted using experimental data for a TRIP/TWIP Fe-22Mn-0.6C steel. The model is able to predict, based on the difference in the stacking fault energies, the activation of TRIP and/or TWIP deformation mechanisms at different temperatures.

1. Introduction

High manganese austenitic steels (15–30 wt% Mn) are particularly attractive for structural applications in the automotive industry because of their outstanding mechanical properties such as high strength and high ductility [1–3]. Under applied loading, the hardening mechanism in this class of steels is due to Transformation Induced Plasticity (TRIP) and/or Twinning Induced Plasticity (TWIP). Austenitic steel systems which exhibit TRIP or TWIP are, for instance, Fe-Mn-C or Fe-Mn-Al-Si [4]. Related alloys where both phenomena can occur concurrently are Fe-Cr-Ni stainless steels which are used in the fields of energy conversion, household and cryogenic applications as well as chemical industries.

Depending on the chemical composition and the deformation temperature, additional plastic deformation mechanisms such as mechanical twinning and/or athermal phase transformation phenomena can occur besides dislocation slip in such steels [4–6]. The activation barriers for these partially competing mechanisms are strongly dependent on the stacking fault energy (SFE) [7]. With decreasing SFE, the plasticity mechanisms change from (i) dislocation glide to (ii) dislocation glide in conjunction with mechanical twinning to (iii) dislocation glide in conjunction with martensitic phase transformation [8]. In general, martensitic transformation is observed in very low SFE steels (below 20 mJ/m^2) while twinning is observed in medium SFE steels (20–40 mJ/m^2). When the SFE exceeds 45 mJ/m^2, dislocation glide becomes the predominant mode of plastic deformation [9].

In this class of steels, the γ-austenite phase is a metastable fcc phase, which can transform into ε-martensite (hcp) or α'-martensite (bcc/bct). Two different transformation paths, $\gamma \rightarrow \varepsilon$ and $\gamma \rightarrow \varepsilon \rightarrow \alpha'$, have been reported [10]. The transformation path is influenced by the Mn content, where the $\gamma \rightarrow \varepsilon$ transformation typically occurs in high Mn steels (15–30 wt% Mn) while the $\gamma \rightarrow \varepsilon \rightarrow \alpha'$ transformation path typically occurs in medium Mn steels (5–12 wt% Mn) [11].

The objective of this work is to develop a physically-based crystal plasticity model for high Mn steels that can capture the activation of different plastic deformation mechanisms, in particular the TRIP and TWIP effects, and their interaction with dislocation plasticity and their respective dependence on the substructure, based on the SFE of the material. The model is implemented within an existing crystal plasticity computational framework, the Düsseldorf Advanced Material Simulation Kit (DAMASK) [12,13].

The twin nucleus model in this paper used to describe deformation twinning was first proposed by Mahajan and Chin [14]. Based on this model, Steinmetz et al. [15] introduced an analytical TWIP model which is an extension of the three internal variable

* Corresponding author.
E-mail address: s.wong@mpie.de (S.L. Wong).

http://dx.doi.org/10.1016/j.actamat.2016.07.032
1359-6454/

model (3IVM) by Roters et al. [16]. This model by Steinmetz et al. [15] is an isotropic model of a polycrystal which does not take grain orientations and grain interactions into account. Jia et al. [17,18] implemented the crystal plasticity-based TWIP model within DAMASK together with dislocation slip and shear banding. In the current study, the TWIP model is extended to also model the $\gamma \rightarrow \varepsilon$ martensitic transformation (TRIP), such that the current constitutive model has the capability to simulate the evolution of dislocation densities, twin volume fractions, and ε-martensite volume fractions. The onset of twinning or martensitic transformation is determined by two separate expressions for the critical stress for twin growth and the critical stress for ε-martensite growth.

In the current work, we restrict our consideration of the martensitic transformation to the $\gamma \rightarrow \varepsilon$ transformation found in high Mn and the related high Ni steels. The $\gamma \rightarrow \varepsilon \rightarrow \alpha'$ transformation which typically occurs in medium Mn and medium Ni steels will be considered in a future study. Therefore the term martensite in this paper will only refer to ε-martensite. The present model does not explicitly account for the precise distribution and arrangement of the twins and martensite laths but rather the volume fraction of twins and ε-martensite at each material point. The focus here is on a modeling approach that enables the prediction of the onset of these different deformation mechanisms based on the SFE and the effect of these competing deformation mechanisms on the hardening behaviour of the material.

This paper is structured as follows: first, existing models for deformation twinning and martensitic phase transformation are reviewed. Next, the model for the twin and ε-martensite nuclei is presented, followed by a detailed description of the constitutive law. The experimental and simulation procedures are next described. Finally, the results and a discussion thereof are presented. The paper ends with some concluding remarks.

2. Previous work

The incorporation of plastic deformation modes such as deformation twinning and martensitic phase transformation in addition to slip within constitutive models has long been an outstanding problem. Early analysis by Chin et al. [19] on the behaviour of crystals subjected to mechanical twinning were based on the adaptation of the Taylor model [20] for mechanical twinning. Van Houtte [21] proposed a simple scheme for reorientation of grains due to twinning during simulation of texture development in a polycrystal. Tome et al. [22] and Lebensohn and Tome [23] proposed twin reorientation and volume fraction transfer schemes for Taylor-type and self-consistent polycrystal models. However, these previous attempts to model the response of polycrystals due to both slip and twinning are for the rigid-plastic, non-hardening case.

Crystal plasticity-based models have also been proposed to model the combined effect of slip and twinning [24,25]. These models have the capability to model strain hardening and texture evolution associated with deformation twinning at the grain scale. Kalidindi [24,26,27] extended the classical crystal plasticity model to include deformation twinning, which was used to model strain hardening and deformation textures in low SFE fcc metals. Kalidindi [27] defined the evolution of the twin volume fraction in the same way as that for slip, using a simple power law and introduced new functions for the slip and twinning resistance. Staroselsky and Anand [25] proposed a phenomenological saturation-type hardening function to capture slip–twin interactions.

Physically-based models for strain hardening and texture evolution have also been introduced [28–31]. Bouaziz and Guelton [30] introduced a physically based model which accounts for the interaction between twinning and dislocation motion by incorporating the characteristic spacing of twins into the dislocation storage. In the model by Allain et al. [31,32], the evolution function of the twin volume fraction is a mathematical description of the twin nucleation, which captures experimental observations of the microstructure. The twin–slip interactions are based on the evolution of the dislocation MPF accounting for the three-dimensional spatial arrangement of twins within a grain.

The modeling of transformation plasticity has also seen a number of developments over the past couple of decades. The drivers for transformation may be controlled by stress (i.e., stress-assisted transformation) or strain (i.e., strain-induced transformation). Olson and Cohen [33] presented a phenomenological model for the kinematics of martensite nucleation in which shear-band intersection is the dominant mechanism for strain-induced martensitic nucleation. The model is based on an estimation of the number of martensite nucleation sites present in the material and the probability of martensite nucleation at these sites. Stringfellow et al. [34] extended the Olson and Cohen model – where the evolution of martensite is related to the plastic strain and temperature – to also account for the effect of the stress state on martensite nucleation. Leblond et al. [35,36] developed a phenomenological model for strain-induced martensitic phase transformation based upon a decomposition of the plastic deformation. A Hill–Mandel homogenization scheme was used to relate the macroscopic stress and strain to the microscopic stresses and strains.

In the literature, several models have been proposed to describe the crystallographic aspects of martensitic transformations using micromechanics approaches [37–43] using a small-strain framework. Suiker and Turteltaub [44–46] developed a model within a multiscale framework to simulate the transformation of fcc austenite into body-centered tetragonal (bct) martensite. This model uses the results from the crystallographic theory of martensitic transformations proposed by Wechsler et al. [47], which was further developed by Ball and James [48] based on the minimization of the free energy.

The models previous described have only considered either the effect of slip and twinning or the effect of slip and transformation. However, models which incorporate the combined effect of slip, deformation twinning and martensitic transformation are more rare. Sun et al. [49] proposed a crystal plasticity model for slip, twinning and transformation induced plastic deformation, using a TWIP steel single crystal for validation.

3. Background

In fcc metals with low SFE, mechanical twinning and ε-martensite nucleation mechanisms are very similar in terms of the dislocation reactions which form the twin and ε-martensite nuclei. In fcc metals, a perfect dislocation on the {111} plane dissociates into two Shockley partial dislocations as follows [50,51]:

$$\frac{a}{2}\left\langle 01\bar{1}\right\rangle + \frac{a}{2}\left\langle 10\bar{1}\right\rangle = 3 \times \frac{a}{6}\left\langle 11\bar{2}\right\rangle \tag{1}$$

where a is the lattice parameter.

Twin formation involves the passage of $\frac{1}{6}\langle 11\bar{2}\rangle$ Shockley partials on every {111} plane [14,52], while the formation of ε-martensite (fcc $\rightarrow$ hcp transformation) is achieved through the passage of $\frac{1}{6}\langle 11\bar{2}\rangle$ Shockley partials on every second {111} plane [53,54].

The twin nucleus model used to describe deformation twinning in the current work was first proposed by Mahajan and Chin [14]. It is a mechanism in which two perfect dislocations split into fault pairs and react on the primary slip plane to produce three Shockley partial dislocations on adjacent planes. A schematic of the twin nucleus based on the model by Mahajan and Chin is shown in

Fig. 1(a). Three stacking faults are on adjacent parallel (111) planes. The straight back lines represent sessile Shockley partial dislocations, while the bowed out front lines represent mobile Shockley partial dislocations. The twins would then form when these three-layer stacking faults inside a slip band on adjacent slip planes grow into one another. The growing twins are assumed to be thin discs where the length and volume of these twins decrease with increasing twin volume fraction.

Mahajan et al. [55] also proposed a similar model for the formation of the ε-martensite nucleus, where instead of the Shockley partials occurring on every {111} plane, the Shockley partials occur on every second {111} plane. The schematic for the ε-martensite nucleus is shown in Fig. 1(b).

Considering first the twin nucleus model depicted in Fig. 1(a), the critical event for growth of the twin nucleus depicted is determined by the overall energy of the system. The total energy of this system is given by Refs. [15,56]:

$$Q_{\text{total}} = Q_{\text{work}} + Q_{\text{sf}} + Q_{\text{line}} \tag{2}$$

The term Q_{total} has three contributions:

$$Q_{\text{work}} = -3b\tau A(r,L) \tag{3}$$

$$Q_{\text{sf}} = \Gamma_{\text{sf}} A(r,L) \tag{4}$$

$$Q_{\text{line}} = \frac{9}{2} Gb^2 B(r,L) \tag{5}$$

where Q_{work} is the energy supplied by the applied shear stress τ, Q_{sf} is the energy required to create two interfaces between the twin and the parent phase, and Q_{line} is the energy required to extend the dislocation line. The term Γ_{sf} represents the stacking fault energy (SFE) and b is the Burgers vector of the Shockley partial. The assumption for Q_{sf} is that the SFE is approximately twice the twin interface energy, Γ_{sf}. The area function $A(r,L)$ and line function $B(r,L)$ for a twin nucleus with dimensions r and L as shown in Fig. 1(a) given as:

$$A(r,L) = \frac{Lr}{4} - \frac{L^3}{16r} + \left(\frac{r^2}{4} + \frac{L^4}{64r^2} + \frac{L^2}{8}\right)\arcsin\left(\frac{4Lr}{L^2+4r^2}\right) \tag{6}$$

$$B(r,L) = \left(r + \frac{L^2}{4r}\right)\arcsin\left(\frac{4Lr}{L^2+4r^2}\right) - L \tag{7}$$

for $r \le L/2$ and

$$A(r,L) = \frac{Lr}{4} - \frac{L^3}{16r} + \left(\frac{r^2}{4} + \frac{L^4}{64r^2} + \frac{L^2}{8}\right)\left(\pi - \arcsin\left(\frac{4Lr}{L^2+4r^2}\right)\right) \tag{8}$$

$$B(r,L) = \left(r + \frac{L^2}{4r}\right)\left(\pi - \arcsin\left(\frac{4Lr}{L^2+4r^2}\right)\right) - L \tag{9}$$

for $r > L/2$, respectively.

For high applied stresses, the energy is constantly decreasing, but for a particular stress level a saddle point is found at $r/L = 0.5$, as shown in Fig. 2(a). The saddle point is very sharp in stress, creating a steep increase in the activation barrier for small reductions in stress, resulting in an essentially athermal barrier stress. At this point, the mobile partial dislocations will have formed a semicircle between the two pinning points. The stress at this configuration is defined as the critical stress for twin growth and is given by:

$$\widehat{\tau}_{\text{tw}} = \frac{\Gamma_{\text{sf}}}{3b_{\text{tw}}} + \frac{3Gb_{\text{tw}}}{L_{\text{tw}}} \tag{10}$$

The hcp nucleus model proposed by Mahajan et al. [55] is used in the present model to describe $\gamma \rightarrow \varepsilon$ martensitic phase transformation. Similar to the twin nucleation model, the critical event for growth of a hcp nucleus is also determined by the overall energy of the system. The expression for the overall energy of the system is similar to Eq. (2), although an additional term Q_{trans} is needed to account for the release in energy due to a change in phase:

$$Q_{\text{total}} = Q_{\text{work}} + Q_{\text{int}} + Q_{\text{line}} + Q_{\text{trans}} \tag{11}$$

For low SFE, the assumption that the SFE is approximately twice the interface energy used in the twinning case in Eq. (4) is no longer valid. Therefore, the interface energy term, Q_{int}, for the transformation case is given as:

$$Q_{\text{int}} = 2\sigma^{\gamma/\varepsilon} A(r,L) \tag{12}$$

where $\sigma^{\gamma/\varepsilon}$ is the interface energy.

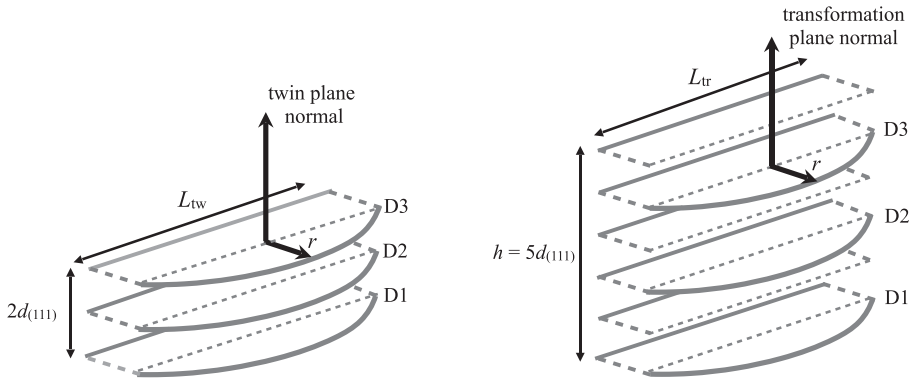

(a) Twin nucleus model by Steinmetz et al. [15] (b) ε-martensite nucleus

Fig. 1. Schematic of the twin and ε-martensite nuclei, where $d_{(111)}$ is the interplanar spacing of the {111} plane, L is the length of the sessile Shockley partial dislocations forming the twin/ε-martensite nucleus, r is the distance the mobile Shockley partial dislocations have bowed out. Three mobile Shockley dislocations which can grow into each other to form a twin or ε-martensite lath are denoted by D_1, D_2 and D_3.

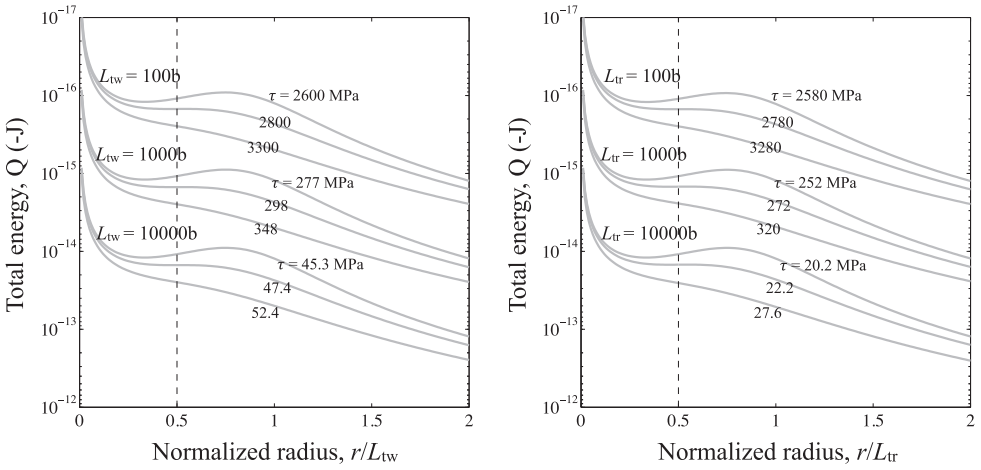

(a) Total energy for twin nucleus (b) Total energy for ε-martensite nucleus

Fig. 2. Total energy, Q_{total} of the twin and ε-martensite nucleus as a function of the normalized radius, r/L. The energy curves were computed using the following values: $G = 93$ GPa, $\Gamma_{sf} = 15$ mJ/m^2, $\sigma^{\gamma/\varepsilon}$=10 mJ/m^2, $b = b_{tw} = b_{tr} = 2.56 \times 10^{-10}$m, $a = 3.68 \times 10^{-10}$m. The numbers on each curve represent the applied shear stress.

The transformation energy term, Q_{trans} is given as:

$$Q_{trans} = hA(r,L)\Delta G^{\gamma\to\varepsilon} \tag{13}$$

where h is the height of the hcp nucleus, $L = L_{tr}$, and $\Delta G^{\gamma\to\varepsilon}$ is the change in Gibbs free energy per unit volume from the austenite to the martensite phase.

The energy curves for ε-martensite (hcp) nucleation are shown in Fig. 2(b), where for the same energy level, the stress required for growth of the ε-martensite nucleus is lower compared to twinning. The critical stress for growth of the hcp nucleus is:

$$\widehat{\tau}_{tr} = \frac{2\sigma^{\gamma/\varepsilon}}{3b_{tr}} + \frac{3Gb_{tr}}{L_{tr}} + \frac{h\Delta G^{\gamma\to\varepsilon}}{3b_{tr}} \tag{14}$$

where b_{tr} is the Burgers vector for transformation.

4. Constitutive law

4.1. Kinematics

The total deformation gradient $\mathbf{F}$ is decomposed into an elastic part, $\mathbf{F}_e$, and a plastic part, $\mathbf{F}_p$ [57]:

$$\mathbf{F} = \mathbf{F}_e\mathbf{F}_p \tag{15}$$

The elastic part $\mathbf{F}_e$ consists of a stretch, $\mathbf{U}_e$ and a lattice rotation, $\mathbf{R}_e$ according to the polar decomposition $\mathbf{F}_e$=$\mathbf{R}_e\mathbf{U}_e$.

The total velocity gradient is defined as:

$$\mathbf{L} = \dot{\mathbf{F}}\mathbf{F}^{-1} \tag{16}$$

The plastic velocity gradient, $\mathbf{L}_p$, in the relaxed configuration for pure dislocation slip is determined by the slip rates $\dot{\gamma}^\alpha$ on all active slip systems α:

$$\mathbf{L}_p = \sum_{\alpha=1}^{N_s} \dot{\gamma}^\alpha \boldsymbol{m}^\alpha \otimes \boldsymbol{n}^\alpha \tag{17}$$

where $\boldsymbol{m}^\alpha$ and $\boldsymbol{n}^\alpha$ are the slip direction and the slip plane normal of slip system α, respectively.

Following the approach of Kalidindi [24], the contribution of mechanical twinning and phase transformation are taken into account as an additional terms in the plastic velocity gradient:

$$\mathbf{L}_p = \left(1 - \sum_{\beta=1}^{N_{tw}} f^\beta - \sum_{\chi=1}^{N_{tr}} f^\chi\right) \sum_{\alpha=1}^{N_s} \dot{\gamma}^\alpha \boldsymbol{m}^\alpha \otimes \boldsymbol{n}^\alpha + \sum_{\beta=1}^{N_{tw}} \dot{\gamma}^\beta \boldsymbol{m}_{tw}^\beta \otimes \boldsymbol{n}_{tw}^\beta + \sum_{\chi=1}^{N_{tr}} \dot{\gamma}^\chi \boldsymbol{m}_{tr}^\chi \otimes \boldsymbol{n}_{tr}^\chi \tag{18}$$

where f^β is the volume fraction of twins for the twin system β and f^χ is the volume fraction of martensite for the transformation system χ. The vectors $\boldsymbol{m}$ and $\boldsymbol{n}$ denote the directions and plane normals of the deformation systems on which shear occurs at a rate of $\dot{\gamma}$.

The present expression for $\mathbf{L}_p$ in Eq. (18) does not consider subsequent slip within twins and ε-martensite. This approximation is often suitable for extremely thin twins, while the ε-martensite is assumed to have a very high yield strength and therefore only deforms elastically after transformation occurs.

Slip occurs on the 12 $\{111\}\langle 110\rangle$ slip systems, while twinning occurs on the 12 $\{111\}\langle 112\rangle$ twin systems. The fcc to hcp lattice transformation in the model is described by the Shoji-Nishiyama orientation relationship [58]:

$$(111)_{fcc} || (0001)_{hcp}$$

$$\left[11\bar{2}\right]_{fcc} || \left(1\bar{1}00\right)_{hcp}$$

An orthonormal basis in the fcc lattice consisting of the directions $[11\bar{2}]$, $[\bar{1}10]$ and [111] becomes $[1\bar{1}00]$, $[11\bar{2}0]$, and [0001] respectively, in the hcp lattice. Assuming that the resulting hcp phase has an ideal c/a ratio, the deformation gradient which transforms the fcc phase to the hcp phase is a simple shear $\sqrt{2}/4$ in the $[11\bar{2}]$fcc direction on the $(111)_{fcc}$ plane:

$$\mathbf{S} = \begin{pmatrix} 1 & 0 & \sqrt{2}/4 \\ 0 & 1 & 0 \\ 0 & 0 & 1 \end{pmatrix} \tag{19}$$

All {111} planes of the fcc lattice are possible shear planes. Each {111} plane contains three ⟨112⟩ shear directions; therefore, there are 12 possible ε-martensite variants. The transformation tensor associated with the transformation system χ, which is analogous to

the Schmidt tensor, is defined as:

$$\mathbf{N}_\chi = \mathbf{R}_\chi \mathbf{S} \mathbf{R}_\chi^T - \mathbf{I} = \boldsymbol{m}_{\mathrm{tr}}^\chi \otimes \boldsymbol{n}_{\mathrm{tr}}^\chi \tag{20}$$

where $\mathbf{R}_\chi$ is the rotation matrix which rotates the orthonormal basis aligned with the fcc lattice to the orthonormal basis aligned with the ⟨112⟩, ⟨110⟩ and ⟨111⟩ directions. The calculated values of $\mathbf{N}_\chi$ for fcc materials is shown in Table 4.1.

χ	$\mathbf{N}_\chi = \mathbf{m}_{\mathrm{tr}}^\chi \otimes \mathbf{n}_{\mathrm{tr}}^\chi$
1	$[\bar{2}11]\otimes(111)/12$
2	$[1\bar{2}1]\otimes(111)/12$
3	$[11\bar{2}]\otimes(111)/12$
4	$[2\bar{1}1]\otimes(\bar{1}11)/12$
5	$[\bar{1}21]\otimes(\bar{1}11)/12$
6	$[\bar{1}\bar{1}2]\otimes(\bar{1}11)/12$
7	$[\bar{2}\bar{1}1]\otimes(1\bar{1}1)/12$
8	$[12\bar{1}]\otimes(1\bar{1}1)/12$
9	$[1\bar{1}2]\otimes(1\bar{1}1)/12$
10	$[21\bar{1}]\otimes(\bar{1}1\bar{1})/12$
11	$[\bar{1}2\bar{1}]\otimes(\bar{1}1\bar{1})/12$
12	$[\bar{1}12]\otimes(\bar{1}1\bar{1})/12$

4.2. Dislocation densities

The microstructure is parameterized in terms of the edge dislocation density, ρ_e, the dipole dislocation density, ρ_d, the twin volume fraction, f_{tw}, and the ε-martensite volume fraction, f_{tr}.

In a dislocation-based model, the Orowan equation [59] gives the shear rate on the slip system α as:

$$\dot{\gamma}^\alpha = \rho_e b_s v_0 \exp\left[-\frac{Q_s}{k_B T}\left\{1-\left(\frac{|\tau_{\mathrm{eff}}^\alpha|}{\tau_{\mathrm{sol}}}\right)^p\right\}^q\right]\mathrm{sign}(\tau^\alpha) \tag{21}$$

where $\tau_{\mathrm{eff}}^\alpha$ is the effective resolved shear stress on the slip system α, τ_{sol} is the solid solution strength, b_s is the length of the Burgers vector for slip, v_0 is the dislocation glide velocity, Q_s is the activation energy for dislocation slip, k_B is the Boltzmann constant, T is the temperature, p and q are fitting parameters.

The effective shear stress, $\tau_{\mathrm{eff}}^\alpha$, is calculated as:

$$\tau_{\mathrm{eff}}^\alpha = \begin{cases} |\tau^\alpha| - \tau_{\mathrm{pass}}^\alpha, & \text{for } |\tau^\alpha| > \tau_{\mathrm{pass}}^\alpha \\ 0, & \text{for } |\tau^\alpha| \le \tau_{\mathrm{pass}}^\alpha \end{cases}$$

where τ^α is the resolved shear stress on the slip system α.

The passing stress, $\tau_{\mathrm{pass}}^\alpha$ is given by:

$$\tau_{\mathrm{pass}}^\alpha = Gb\left(\sum_{\alpha'=1}^{N_s} \xi_{\alpha\alpha'}\left(\rho_e^{\alpha'} + \rho_d^{\alpha'}\right)\right)^{1/2} \tag{22}$$

where G is the shear modulus, $\xi_{\alpha\alpha'}$ is interaction matrix between the different slip systems α and α'.

The evolution of the edge dislocation density is given as:

$$\dot{\rho}_e^\alpha = \frac{|\dot{\gamma}^\alpha|}{b_s \Lambda_s^\alpha} - \frac{2\hat{d}^\alpha}{b_s}\rho_e^\alpha|\dot{\gamma}^\alpha| - \frac{2d^\alpha}{b_s}\rho_e^\alpha|\dot{\gamma}^\alpha| \tag{23}$$

where Λ_s^α is the mean free path (MFP) for slip which will be described in Section 4.3.

The evolution of the dislocation dipole density is given as:

$$\dot{\rho}_d^\alpha = \frac{2\hat{d}^\alpha}{b_s}\rho_e^\alpha|\dot{\gamma}^\alpha| - \frac{2d^\alpha}{b_s}\rho_d^\alpha|\dot{\gamma}^\alpha| - \rho_d^\alpha\frac{4v_{\mathrm{climb}}}{\left(\hat{d}^\alpha - d^\alpha\right)} \tag{24}$$

The dislocation climb velocity is given as:

$$v_{\mathrm{climb}} = \frac{3GD_0\Omega}{2\pi k_B T}\frac{1}{\left(\hat{d}^\alpha + d^\alpha\right)}\exp\left(-\frac{Q_c}{k_B T}\right) \tag{25}$$

where D_0 is the self-diffusion coefficient for fcc Fe, Ω is the activation volume for climb and Q_c is the activation energy for climb.

The maximum glide plane distance two dislocations can have to form a dipole, $\hat{d}^\alpha$ and the minimum distance required for two edge dislocations to annihilate, d^α, are calculated respectively as:

$$\hat{d}^\alpha = \frac{3Gb_s}{16\pi|\tau^\alpha|} \tag{26}$$

$$d^\alpha = C_{\mathrm{anni}} b_s \tag{27}$$

where C_{anni} is a fitting parameter.

4.3. Mean free paths

Strain hardening is described in terms of a dislocation mean free path (MFP) approach, where the mean free path is denoted by the symbol Λ. The mean free path for slip has confining contributions due to the pileup of dislocations, the formation of twins and the formation of ε-martensite as follows:

$$\frac{1}{\Lambda_s^\alpha} = \frac{1}{d} + \frac{1}{\lambda_{\mathrm{slip}}^\alpha} + \frac{1}{\lambda_{\mathrm{sliptwin}}^\alpha} + \frac{1}{\lambda_{\mathrm{sliptrans}}^\alpha} \tag{28}$$

$$\frac{1}{\lambda_{\mathrm{slip}}^\alpha} = \frac{1}{i_{\mathrm{slip}}}\left(\sum_{\alpha'=1}^{N_s} \xi_{\alpha\alpha'}\left(\rho_{\mathrm{edge}}^{\alpha'} + \rho_{\mathrm{dipole}}^{\alpha'}\right)\right)^{1/2} \tag{29}$$

$$\frac{1}{\lambda_{\mathrm{sliptwin}}^\alpha} = \sum_{\beta=1}^{N_{\mathrm{tw}}} \xi_{\alpha\beta} f^\beta \frac{1}{t_{\mathrm{tw}}(1-f_{\mathrm{tw}})} \tag{30}$$

$$\frac{1}{\lambda_{\mathrm{sliptrans}}^\alpha} = \sum_{\chi=1}^{N_{\mathrm{tr}}} \xi_{\alpha\chi} f^\chi \frac{1}{t_{\mathrm{tr}}(1-f_{\mathrm{tr}})} \tag{31}$$

where d is the average grain size, t_{tw} is the average twin thickness, t_{tr} is the average ε-martensite thickness, f_{tw} is the total twin volume fraction, f_{tr} is the total ε-martensite volume fraction and i_{slip} is a fitting parameter. $\xi_{\alpha\alpha'}$ is the interaction matrix between the different slip systems α and α', $\xi_{\alpha\beta}$ is the interaction matrix between the slip system α and twin system β and $\xi_{\alpha\eta}$ is the interaction matrix between the slip system α and transformation system χ.

The mean free path between two obstacles seen by a growing twin is computed as:

$$\frac{1}{\Lambda_{\mathrm{tw}}^\beta} = \frac{1}{i_{\mathrm{tw}}}\left(\frac{1}{d} + \sum_{\beta'=1}^{N_{\mathrm{tw}}} \xi_{\beta\beta'} f^{\beta'} \frac{1}{t_{\mathrm{tw}}(1-f_{\mathrm{tw}})}\right) \tag{32}$$

where i_{tw} is a fitting parameter and $\xi_{\beta\beta'}$ is the interaction matrix between the different twin systems β and β'.

The mean free path between two obstacles seen by a growing ε-martensite lath is computed as:

$$\frac{1}{\Lambda_{tr}^{\chi}} = \frac{1}{i_{tr}}\left(\frac{1}{d} + \sum_{\chi'=1}^{N_{tr}} \xi_{\chi\chi'} f^{\chi'} \frac{1}{t_{tr}(1-f_{tr})}\right) \tag{33}$$

where i_{tr} is a fitting parameter and $\xi_{\chi\chi'}$ is the interaction matrix between the different transformation systems χ and χ'.

4.4. Twin nucleation

The twin nucleation rate for the twin system β is given as:

$$\dot{N}_{tw}^{\beta} = \dot{N}_0 p_{ncs} p_{tw} \tag{34}$$

where $\dot{N}_0$ is the number density of potential twin nuclei per unit time.

The probability that cross-slip does not occur, which would allow a sufficient number of dislocations to pile up and form the stress concentration necessary to form a twin nucleus, is given as:

$$p_{ncs} = 1 - \exp\left[-\frac{V_{cs}}{k_B T}\left(\tau_r - \tau^{\beta}\right)\right] \tag{35}$$

where V_{cs} is the cross-slip activation volume.

The stress needed to bring two partials to within the critical distance to form the twin nucleus, x_c, without help from an external applied shear stress is:

$$\tau_r = \frac{Gb}{2\pi(x_0 + x_c)} + \frac{Gb\cos(\pi/3)}{2\pi x_0} \tag{36}$$

The equilibrium separation of Shockley partials in fcc metals is calculated as:

$$x_0 = \frac{G}{\Gamma_{sf}} \frac{b^2}{8\pi} \frac{2+\nu}{1-\nu} \tag{37}$$

The probability that the twin nucleus shown in Fig. 1(a) bows out to form a twin is:

$$p_{tw} = \exp\left[-\left(\frac{\widehat{\tau}_{tw}}{\tau^{\beta}}\right)^{A}\right] \tag{38}$$

where the critical stress for twinning, $\widehat{\tau}_{tw}$, is given in Eq. (10), τ^{β} is the resolved shear stress on the twin system β and A is a fitting parameter which determines the sharpness of the transition between the non-twinning to the twinning regime.

The evolution of the twin volume fraction is expressed as:

$$\dot{f}^{\beta} = (1 - f_{tw} - f_{tr}) V^{\beta} \dot{N}_{tw}^{\beta} \tag{39}$$

where $f_{tw} = \sum_{\beta=1}^{N_{tw}} f^{\beta}$ and $f_{tr} = \sum_{\chi=1}^{N_{tr}} f^{\chi}$.

The resulting shear rate for each twin system β is calculated as

$$\dot{\gamma}^{\beta} = \gamma_{tw} \dot{f}^{\beta} \tag{40}$$

where γ_{tw} is the characteristic twin shear.

The volume of a new twin is:

$$V^{\beta} = \frac{\pi}{4} \Lambda_{tw}^2 t_{tw} \tag{41}$$

where Λ_{tw} is given in Eq. (32) and t_{tw} is the average twin thickness.

4.5. ε-martensite nucleation

The probability that the six layer hcp nucleus bows out to form an ε-martensite lath is:

$$p_{tr} = \exp\left[-\left(\frac{\widehat{\tau}_{tr}}{\tau^{\chi}}\right)^{B}\right] \tag{42}$$

where the critical stress for transformation, $\widehat{\tau}_{tr}$ is given in Eq. (14), τ^{χ} is the resolved shear stress on the transformation system χ and B is a fitting parameter.

The total nucleation rate of ε-martensite is given as:

$$\dot{N}_{tr}^{\chi} = \dot{N}_0 p_{ncs} p_{tr} \tag{43}$$

The expression for $\dot{N}_0$ in Eq. (43) is assumed to be the same as that in Eq. (34) because the dislocation reactions are assumed to be equally likely to form twin nuclei or ε-martensite nuclei. The probability p_{ncs} approaches 1.0 as the temperature decreases because cross slip does not occur at low temperatures.

The evolution of the volume fraction of ε-martensite is expressed as:

$$\dot{f}^{\chi} = (1 - f_{tw} - f_{tr}) V^{\chi} \dot{N}_{tr}^{\chi} \tag{44}$$

The volume of the new ε-martensite lath is given by:

$$V^{\chi} = \frac{\pi}{4} \Lambda_{tr}^2 t_{tr} \tag{45}$$

where Λ_{tr} given in Eq. (33) and t_{tr} is the ε-martensite mean thickness.

The shearing rate for each transformation system χ is thus calculated as:

$$\dot{\gamma}^{\chi} = \gamma_{tr} \dot{f}^{\chi} \tag{46}$$

where γ_{tr} is a characteristic shear for transformation.

5. Experimental procedure

The material used in this study is Fe-22Mn-0.6C, where the composition in wt.% is given in Table 1 [60]. Electron backscatter diffraction (EBSD) was used to analyze the texture and microstructure of the as-delivered material, as shown in Fig. 3. Tensile samples were machined using water jet cutting from the as-delivered cold rolled sheet. The tensile samples were annealed at 800 °C for 30 min and subsequently water quenched, resulting in an equiaxed microstructure with an average grain size of 5 μm. Tensile tests were carried out within a temperature range of 123 K–423 K and at a quasi-static initial strain rate of 0.001 s^{-1}. Since tensile tests at 673 K and 773 K were only carried out on the as-delivered material, the Hall-Petch relationship [61] was used to determine the macroscopic stress-strain curves at 673 K and 773 K for the annealed material.

High energy synchrotron x-ray diffraction (XRD) was used to study the evolution of the ε-martensite fraction and EBSD analysis was used to determine the twin volume fraction. The twin volume fraction of the material was determined from EBSD measurements prior to fracture of each sample while the ε-martensite volume fraction was measured in pre-strained tensile samples at macroscopic strains of 0.05, 0.10, 0.20, 0.30, 0.40 and also after fracture of the specimen.

The XRD measurements were carried out at beamline 9 at the

Table 1
Composition of material considered in this study in wt% [60].

Fe	Mn	C	Si	P	S	Cr	Ni	N	Al	Nb	V
76.31	22.50	0.580	0.235	0.022	0.001	0.070	0.030	0.026	0.002	0.0087	0.225

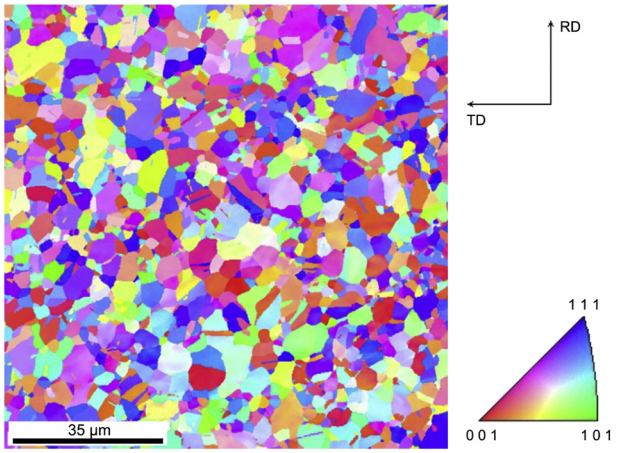

Fig. 3. EBSD map of the as-delivered Fe-22Mn-0.6C cold rolled sheet.

DELTA synchrotron facility in Dortmund, Germany. The measurements were conducted using monochromatic x-rays with a wavelength of $\lambda = 0.45919$ Å and energy of 27 keV. The pre-strained tensile specimens were measured in the Bragg-Brentano configuration with an angle of 2° and a sample to detector distance of 339 mm. A MAR345 2D detector with a resolution of 3450 × 3450 pixels was used to record the diffraction pattern. Prior to each measurement, a calibration measurement was performed on silicon to determine the center of the detector and the sample to detector distance. The diffraction pattern for each sample was then captured using an exposure time of 90 s. The diffraction patterns were then transformed by integrating the intensity of each detection point on a ring into a 1D diagram which plots the intensity versus the 2θ angle. The volume fractions of γ-austenite and ε-martensite phases were calculated using the lattice parameter proposed by Gebhardt et al. [62]. The calculation of the volume fraction was performed by integrating the intensities of the $\gamma(200)$ and $\varepsilon(101)$ peaks using the Rietveld method [63–65]. The ε-martensite volume fraction can be deduced directly from the integrated intensities of the ε-martensite peaks. The experimental procedure has been described in more detail by Twardowski [60].

EBSD measurements were carried out to show the trend in the evolution of twinning with respect to temperature. Since the EBSD measurements were carried using a step size of 50 nm, it was only possible to detect twin lamella or twin bundles larger than 50 nm. The measured quantity in the EBSD analysis is the twin boundary length. The twin volume fraction is approximated by calculating the minimum twin thickness as a function of the stacking fault energy and the mean free path [32]. The procedure of the evaluation of the twin volume fraction is described in Ref. [60].

6. Simulations

Using the constitutive law outlined in Section 4, representative volume element (RVE) simulations were conducted using the spectral solver implemented in the freeware crystal plasticity micromechanical simulation framework DAMASK [12,13]. The RVE is a spectral grid of dimensions 16 × 16 × 16 comprising 100 grains, where the grain shapes were generated using the Voronoi tessellation method. Periodic boundary conditions were applied to this RVE. Mechanical loading on the RVE was imposed by uniaxial tension with the same strain rate of 0.001 s^{-1} as in the experiment. The material was assumed to have a uniform texture and the crystallographic orientations of the grains were randomly assigned from a uniform orientation distribution.

The constitutive parameters for the crystal plasticity model were determined by fitting the macroscopic stress–strain (σ vs. ε) and the strain hardening ($d\sigma/d\varepsilon$ vs. ε) curves obtained from the uniaxial tension experiments. The constitutive parameters used in the simulations are shown in Table 1. Since different strain hardening behaviors were observed for the lower temperature stress-strain curves in comparison to the high temperature curves, it was found that a different value of i_{slip} was required for the high temperature stress-strain curves exhibiting only pure slip (673 K and 773 K). The parameter i_{slip} from Eq. (29) is a scaling factor for the mean free path of dislocations.

The determination of the single crystal elastic moduli for both the austenite and ε-martensite phase is described in Section 6.1. The remaining constitutive model parameters, which are temperature dependent, are described in Section 6.2. The temperature dependent input parameters are the solid solution strength (τ_{sol}), the stacking fault energy (Γ_{sf}), and the Gibbs free energy difference for the $\gamma \rightarrow \varepsilon$ transformation ($\Delta G^{\gamma \rightarrow \varepsilon}$). Since the yield strength of the material varies as a function of temperature, the solid solution strength, τ_{sol}, was also varied to achieve this difference in the simulated stress-strain curves. The values of τ_{sol} used for each temperature are shown in Table 4.

6.1. Single crystal elastic moduli

While the fcc single crystal elastic constants for the austenite phase in Fe-22Mn-0.6C steel can be estimated from the ab initio calculations of Music et al. [66] for Fe-Mn alloys, the hcp single crystal elastic constants for the ε-martensite phase are not available in the literature and are more challenging to calculate. Thus, the single crystal elastic constants for the ε-martensite phase are computed from the fcc elastic constants using the procedure originally proposed by Martin [67,68]. According to this procedure, the fcc and hcp structures can both be constructed from tetrahedral building blocks. The fcc structure is formed by aligning these tetrahedra in equivalent orientations, whereas in the hcp structure these tetrahedra are alternately aligned in two inequivalent orientations that are rotated 180° with respect to each other. The only other difference of the two structures is that the tetrahedral blocks in hcp are distorted from the ideal tetrahedra of fcc.

The cubic elastic constants are first rotated from the [100], [010] and [001] directions which form an orthonormal basis for the fcc crystal lattice to the orthonormal basis represented by the [110], [112] and [111] directions:

$$\begin{aligned}
\overline{C}_{11} &= \frac{1}{2}\left(C^{F}_{11} + C^{F}_{12} + 2C^{F}_{44}\right)\\
\overline{C}_{12} &= \frac{1}{6}\left(C^{F}_{11} + 5C^{F}_{12} - 2C^{F}_{44}\right)\\
\overline{C}_{33} &= \frac{1}{3}\left(C^{F}_{11} + 2C^{F}_{12} + 4C^{F}_{44}\right)\\
\overline{C}_{13} &= \frac{1}{3}\left(C^{F}_{11} + 2C^{F}_{12} - 2C^{F}_{44}\right)\\
\overline{C}_{44} &= \frac{1}{3}\left(C^{F}_{11} - 2C^{F}_{12} + C^{F}_{44}\right)\\
\Delta = \overline{C}_{14} &= \frac{1}{3\sqrt{2}}\left(C^{F}_{11} - C^{F}_{12} - 2C^{F}_{44}\right)
\end{aligned} \tag{47}$$

where the superscripts F and H denote the elastic constants for the fcc phase and hcp phase, respectively.

The conversion from cubic to hexagonal elastic constants is then completed by using two internal strain corrections, X_1 and X_2 as follows:

$$\begin{aligned}
C^{H}_{11} &= \overline{C}_{11} - X_1\\
C^{H}_{12} &= \overline{C}_{12} + X_1\\
C^{H}_{13} &= \overline{C}_{13}\\
C^{H}_{33} &= \overline{C}_{33}\\
C^{H}_{44} &= \overline{C}_{44} - X_2
\end{aligned} \tag{48}$$

where

$$X_1 = \frac{\Delta^2}{\overline{C}_{44}}$$

$$X_2 = \frac{2\Delta^2}{\overline{C}_{11} - \overline{C}_{12}}$$

The single crystal elastic constants for the austenite phase [66] and the computed elastic constants for the ε-martensite phase are shown in Table 3.

Table 3
Single crystal elastic constants for austenite (fcc) and ε-martensite (hcp) used in the simulations.

Austenite (fcc)	$C^{F}_{11} = 175.0$ GPa
	$C^{F}_{12} = 115.0$ GPa
	$C^{F}_{44} = 135.0$ GPa
ε-martensite (hcp)	$C^{H}_{11} = 242.3$ GPa
	$C^{H}_{12} = 117.7$ GPa
	$C^{H}_{13} = 45.0$ GPa
	$C^{H}_{33} = 315.0$ GPa
	$C^{H}_{44} = 40.5$ GPa

6.2. Stacking fault energy

The stacking fault energy (SFE), is defined as [69,70]:

$$\Gamma_{sf} = 2\rho\Delta G^{\gamma\rightarrow\varepsilon} + 2\sigma^{\gamma/\varepsilon} \tag{49}$$

where $\Delta G^{\gamma\rightarrow\varepsilon}$ is the Gibbs free energy difference for the austenite to ε-martensite transformation, and $\sigma^{\gamma/\varepsilon}$ is the interfacial energy between the austenite and ε-martensite phase. The interface energy term is typically treated as a free parameter that is adjusted to better match the experimental data. The interface energy term, $\sigma^{\gamma/\varepsilon}$, is generally taken to be between 5 and 15 mJ/m^2 for transition metals [9,70,71].

The molar surface density, ρ, of the {111} plane is defined as:

$$\rho = \frac{4}{\sqrt{3a^2}}\frac{1}{N_A} \tag{50}$$

where a is the fcc lattice parameter of the austenite phase and N_A is Avogadro's number.

The SFE for the material used in this study is calculated using the thermodynamic approach by Dumay et al. [72] using the composition shown in Table 1. The calculated values of the SFE at each temperature are shown in Table 4. It is known that the SFE for Fe-22Mn-0.6C steel at room temperature is typically in the range of 20–25 mJ/m^2 and that the transition between the TRIP and TWIP regimes occurs approximately at 20 mJ/m^2 [72]. However, when the SFE is below 12 mJ/m^2, α'-martensite is predominant rather than

Table 2
Input parameters for the constitutive model.

	Symbol	Description	Value	Units
Slip parameters parameters	b_s	Burgers vector for slip	2.56×10^{-10}	m
	Q_s	Activation energy for slip	3.5×10^{-19}	J
	Q_c	Activation energy for climb	3.0×10^{-19}	J
	Ω	Activation volume for climb	$1.5b_s^3$	m^3
	p	Top of the obstacle profile	1.15	
	q	Bottom of the obstacle profile	1.0	
	i_{slip}	Average dislocation spacings a discloation travels	30.0	
	v_0	Dislocation glide velocity	1.0×10^{-4}	m/s
	D_0	Self-diffusion coefficient for fcc Fe	4.0×10^{-5}	m^2/s
	C_{anni}	Coefficient for dislocation annihilation	2.0	
	d	Grain size	5.0	μm
Twin parameters parameters	b_{tw}	Burgers vector for twinning	1.20×10^{-10}	m
	L_{tw}	Width of twin nucleus	1.92×10^{-7}	m
	i_{tw}	Average twin spacings a dislocation travels	10.0	
	t_{tw}	Average twin thickness	5.0×10^{-8}	m
	A	Twinning transition profile width exponent	5.0	
	V_{cs}	Cross-slip activation volume	1.67×10^{-29}	m^3
Transformation parameters	b_{tr}	Burgers vector for transformation	1.47×10^{-10}	m
	L_{tr}	Width of martensite nucleus	1.28×10^{-7}	m
	i_{tr}	Average martensite spacings a dislocation travels	3.0	
	t_{tr}	Average martensite thickness	1.0×10^{-7}	m
	B	Transformation transition profile width exponent	8.0	

Table 4
Temperature-dependent input parameters. The solid solution strength, τ_{sol}, is determined from fitting the experimental stress-strain curves shown in Fig. 4. The SFE (Γ_{sf}) and the Gibbs free energy ($\Delta G^{\gamma\to\varepsilon}$) are calculated using the approach by Dumay et al. [72], assuming the interface energy ($\sigma^{\gamma/\varepsilon}$) values as shown in this table.

Temperature (K)	τ_{sol} (MPa)	Γ_{sf} (mJ/m^2)	$\Delta G^{\gamma\to\varepsilon}$ (J/mol)	$\sigma^{\gamma/\varepsilon}$ (mJ/m^2)
123	250	14.33	−266.25	15
233	160	19.45	−9.42	10
293	130	25.37	91.30	10
373	130	39.03	323.32	10
423	100	48.60	486.02	10
673	60	98.32	1330.78	10
773	35	118.41	1672.13	10

ε-martensite [73]. It was observed found from the experimental measurements that the type of martensite found in the material was predominantly ε-martensite. Therefore, the SFE at 123 K and 233 K should be larger than 12 mJ/m^2. Using an interface energy value of $\sigma^{\gamma/\varepsilon}$=10 mJ/m^2 in Eq. (49) satisfies this condition.

However, using an interface energy value of $\sigma^{\gamma/\varepsilon}$=10 mJ/m^2, the simulated ε-martensite volume fraction did not compare well with the experimentally measured values at 123 K. A better fit between the experimental and simulated data was obtained at 123 K using a $\Delta G^{\gamma\to\varepsilon}$ value that is more negative than the one obtained using an interface energy value of $\sigma^{\gamma/\varepsilon}$=10 mJ/m^2. The SFE is difficult to calculate accurately at low temperatures because of the difficulty in determining the magnetic contribution to the SFE at these temperatures [74]. The SFE calculated using Density Functional Theory (DFT) methods for Fe-Mn alloys are largely negative [75] and the extrapolation of SFE to low temperatures results in values of the SFE not lower than −40 mJ/m^2. This large discrepancy indicates that magnetic interactions and/or chemical ordering play a crucial role in Fe-Mn alloys and have to be taken into account in the computation of the SFE, which is beyond the scope of the current study.

7. Results

The experimental stress-strain curves are shown in Fig. 4. These stress-strain curves show two different types of strain hardening behaviour depending on the temperature regime. The stress-strain curves in the temperature regime of 123 K–423 K have the same slope in the plastic regime and differ only in the yield stress, where the yield stress increases with decreasing temperature [1,2,8]. However, the high temperature stress-strain curves (673 K and 773 K) have a smaller slope compared to the lower temperature curves (123 K–423 K) and therefore exhibit less strain hardening.

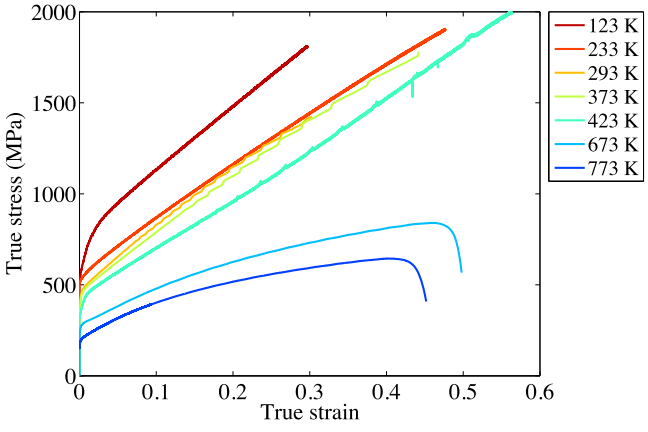

Fig. 4. Experimental stress-strain curves at different temperatures.

The stress-strain curves at 673 K and 773 K exhibit only pure slip and therefore the addition of the TRIP and TWIP effect increases the rate of strain hardening for the lower temperature curves.

The comparison between the experimental and simulated stress-strain curves is shown in Fig. 5(a), while the comparison between the experimental and simulated hardening curves is shown in Fig. 5(b). The hardening curves are calculated as the slope ($d\sigma/d\varepsilon$) of the stress-strain curves. The simulated stress-strain curves fit reasonably well to the experimental data. The strain hardening curves compare less well, however, the hardening curves calculated from the experimental stress-strain data are relatively noisy. To reduce noise in the experimental stress-strain data, the stress-strain curves were smoothed using a moving average of 40 data points. It was checked that the smoothing procedure did not remove important trends from the stress-strain data. The hardening curves in Fig. 5(b) were then determined based on the smoothed stress-strain curves.

The comparison of the measured and simulated twin volume fractions is shown in Fig. 5(c). There is qualitative agreement between the measured and computed twin volume fractions, where twinning decreases with decreasing temperature. Although the computed twin volume fraction at 123 K is not zero as in the experiment, the computed twin volume fraction is very small. However, the model tends to overpredict the twin volume fractions at 373 K and 423 K while slightly under predicting the twin volume fractions at 233 K and 293 K. Although the twin volume fractions were not measured for the high temperature curves at 673 K and 773 K, the model predicts that there twinning does not occur at those temperatures, which is expected at high temperatures [15,76].

For the ε-martensite volume fractions shown in Fig. 5(d), the measured and computed volume fractions decrease with increasing temperature. The martensitic transformation is more active at lower temperatures because of the lower SFE and more difficulties for cross-slip of the material. Martensitic phase transformation decreases at higher temperatures as the SFE and Gibbs free energy increases. Above 233 K, the ε-martensite volume fraction is on the order of 0.05.

8. Discussion

Serrations are observed in the experimental stress-strain curves in Fig. 4 at temperatures of 293 K, 373 K and 423 K. This jerky or serrated behaviour in the stress-strain curves has also been observed in TWIP steels [77–79] and has been attributed to the Portevin–Le Chatelier effect, a type of dynamic strain aging (DSA). The presence of twins in the material act as obstacles to plastic flow [80]. When dislocation meets obstacles (like twins) they are temporary arrested. During this time solutes (such as interstitial particles) diffuse around the dislocations further strengthening the obstacles. Eventually, when the applied stress is sufficiently high these dislocations will overcome these obstacles and will quickly move to the next obstacle where they are stopped and the process is repeated.

It should be noted that in the experiments, the twin volume fraction of a sample just prior to fracture is measured using EBSD. This means that only one data point is available for the twin volume fraction at each temperature, as seen in Fig. 5(c). Since only the twin volume fraction prior to fracture is known, the evolution path of the twin volume fraction with increasing strain is not known.

The onset of plastic deformation mechanisms such as slip, twinning and martensitic phase transformation is controlled by the critical resolved shear stresses for slip, twinning and martensitic phase transformation, respectively. However, the yield strength of the material also increases with decreasing temperature which

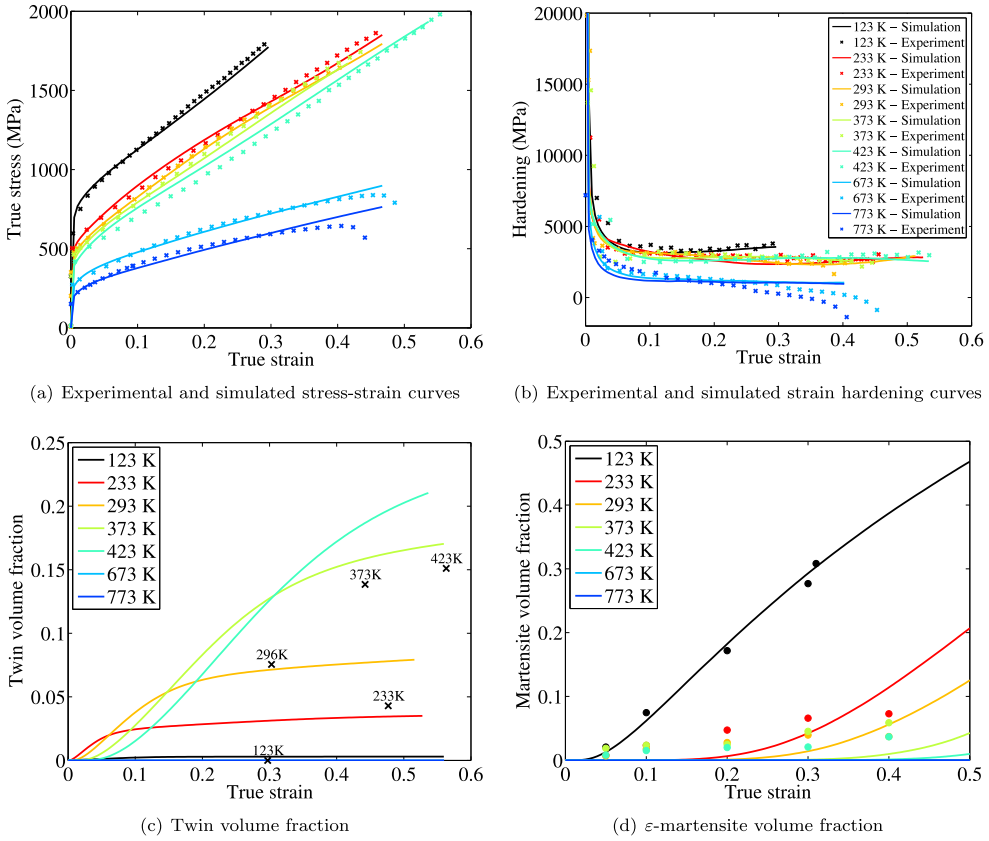

(a) Experimental and simulated stress-strain curves

(b) Experimental and simulated strain hardening curves

(c) Twin volume fraction

(d) ε-martensite volume fraction

Fig. 5. Comparison between experimental and simulation data.

means that the influence of temperature has to be taken into account within the model on both the solid solution strength and the SFE. As shown in the previous section, the model tends to over predict the twin volume fraction at 373 K and 423 K. Since the model is highly dependent on the SFE to predict the onset of twinning and martensitic phase transformation, accurate determination of the SFE is important. In this study, however, since the SFE is calculated using a CALPHAD approach [9,72], it is possible that there are some inaccuracies in determining the SFE particularly at low temperatures. While there are still improvements to be made in terms of accurately determining the SFE for use in the model, it should be emphasized that the goal of this model is to predict the activation of the TRIP and/or TWIP effects within different temperature or stacking fault energy regimes. Alternatively, the current model could also be validated at room temperature through a study varying the SFE of the material by varying the composition.

A numerical study was conducted in this work where the SFE was varied at room temperature (293 K) to investigate the influence of the SFE on the twin volume fractions and ε-martensite volume fraction at a constant temperature of 293 K. The constitutive parameters that were used in this study are shown in Table 2.

Using the current model, the effect of varying the SFE at a constant temperature on the evolution of the twin volume fraction can be investigated, as shown in Fig. 6. At SFE values below 20 mJ/m^2, twinning does not occur. The twin volume fraction increases with increasing SFE up to 50 mJ/m^2. Above 50 mJ/m^2, twinning decreases with increasing SFE. This indicates that twinning occurs at intermediate values of the SFE and there is less tendency for twinning to occur at low or high values of the SFE.

The effect of varying the SFE at a constant temperature of 293 K

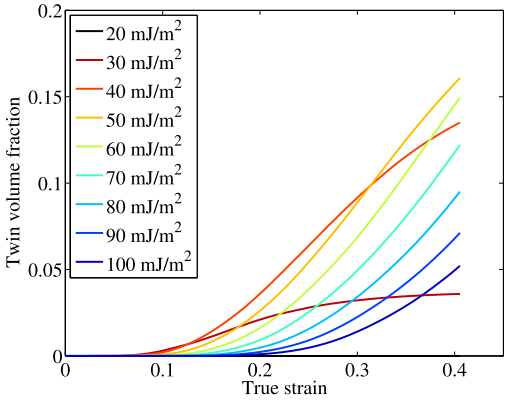

Fig. 6. Evolution of twin volume fraction for different SFEs at a constant temperature of 293 K.

on the ε-martensite volume fraction is shown in Fig. 7. Using the TRIP model, it is observed that as the SFE increases, the formation of ε-martensite decreases. This is consistent with the observation that martensitic phase transformation tends to occur at low SFE values. By increasing the distance between the pinning points of the ε-martensite nucleus, L_{tr}, the onset of phase transformation can be controlled as well.

9. Conclusion

A martensitic phase transformation model has been developed within a crystal plasticity framework to simulate the $\gamma \rightarrow \varepsilon$

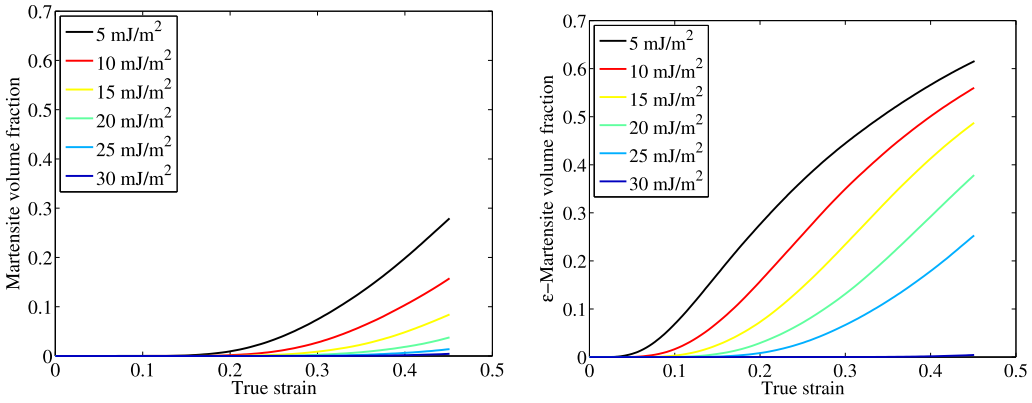

(a) $B = 15,\ L_{\mathrm{tr}} = 500b_s$ (b) $B = 15,\ L_{\mathrm{tr}} = 750b_s$

Fig. 7. Evolution of ε-martensite volume fraction for different SFEs at a constant temperature of 293 K.

transformation in high Mn and high Ni base steels. The novelty of this model is that martensitic phase transformation is incorporated in addition to dislocation glide and twinning. By conducting FFT-based crystal plasticity simulations using the spectral solver within DAMASK, quantitative comparisons are conducted between the experiments and simulations on the stress-strain curves, strain hardening curves, twin volume fraction and ε-martensite for a Fe-22Mn-0.6C steel.

The model is able to predict, based on the temperature, which in turn changes the stacking fault energy of the material, the activation of martensitic phase transformation at low temperatures, the predominance of twinning at intermediate temperatures, and plastic deformation solely by pure slip at high temperatures. It is observed from the experiments that $\gamma \rightarrow \varepsilon$ transformation occurs at low temperatures and increases as the temperature decreases. However, twinning occurs starting at room temperature and increases as the temperature increases.

Acknowledgements

The authors gratefully acknowledge the financial support of the Deutsche Forschungsgemeinschaft (DFG) within the Collaborative Research Center (SFB) 761 “Steel-ab initio”.

References

[1] O. Grässel, L. Krüger, G. Frommeyer, L.W. Meyer, High strength Fe–Mn–(Al, Si) TRIP/TWIP steels development — properties — application, Int. J. Plasticity 16 (10–11) (2000) 1391–1409.
[2] G. Frommeyer, U. Brüx, P. Neumann, Supra-ductile and high-strength manganese-TRIP/TWIP steels for high energy absorption purposes, ISIJ Int. 43 (3) (2003) 438–446.
[3] L. Krüger, L.W. Meyer, U. Brüx, G. Frommeyer, O. Grässel, Stress-deformation behaviour of high manganese (Al, Si) TRIP and TWIP steels, J. de Physique IV 110 (2003) 189–194.
[4] D.T. Pierce, J.A. Jiménez, J. Bentley, D. Raabe, C. Oskay, J.E. Wittig, The influence of manganese content on the stacking fault and austenite/-martensite interfacial energies in Fe–Mn–(Al–Si) steels investigated by experiment and theory, Acta Mater. 68 (2014) 238–253.
[5] L. Remy, A. Pineau, Twinning and strain-induced F.C.C. → H.C.P. transformation in the Fe-Mn-Cr-C system, Mater. Sci. Eng. 28 (1) (1977) 99–107.
[6] S. Martin, S. Wolf, U. Martin, L. Krüger, D. Rafaja, Deformation mechanisms in austenitic TRIP/TWIP steel as a function of temperature, Metallurgical Mater. Trans. A 47 (1) (2016) 49–58.
[7] H. Idrissi, L. Ryelandt, M. Veron, D. Schryvers, P.J. Jacques, Is there a relationship between the stacking fault character and the activated mode of plasticity of Fe–Mn-based austenitic steels? Scr. Mater. 60 (11) (2009) 941–944.
[8] S. Curtze, V.-T. Kuokkala, Dependence of tensile deformation behavior of TWIP steels on stacking fault energy, temperature and strain rate, Acta Mater. 58 (15) (2010) 5129–5141.
[9] S. Allain, J.-P. Chateau, O. Bouaziz, S. Migot, N. Guelton, Correlations between the calculated stacking fault energy and the plasticity mechanisms in Fe–Mn–C alloys, Mater. Sci. Eng. A 387–389 (2004) 158–162.
[10] A. Sato, K. Soma, T. Mori, Hardening due to pre-existing ε-Martensite in an Fe-30Mn-1Si alloy single crystal, Acta Metall. 30 (10) (1982) 1901–1907.
[11] U. Prahl, W. Bleck, A. Saeed-Akbari, Steel–Ab initio: quantum mechanics guided design of new Fe-Based materials, in: Proceedings of the 2nd World Congress on Integrated Computational Materials Engineering (ICME), 2013, pp. 37–42.
[12] http://damask.mpie.de.
[13] F. Roters, P. Eisenlohr, C. Kords, D. Tjahjanto, M. Diehl, D. Raabe, DAMASK: the Düsseldorf Advanced MAterial Simulation Kit for studying crystal plasticity using an FE based or a spectral numerical solver, Procedia IUTAM 3 (2012) 3–10.
[14] S. Mahajan, G. Chin, Formation of deformation twins in f.c.c. crystals, Acta Metall. 21 (10) (1973) 1353–1363.
[15] D.R. Steinmetz, T. Jäpel, B. Wietbrock, P. Eisenlohr, I. Gutierrez-Urrutia, A. Saeed-Akbari, T. Hickel, F. Roters, D. Raabe, Revealing the strain-hardening behavior of twinning-induced plasticity steels: theory, simulations, experiments, Acta Mater. 61 (2) (2013) 494–510.
[16] F. Roters, D. Raabe, G. Gottstein, Work hardening in heterogeneous alloys—a microstructural approach based on three internal state variables, Acta Mater. 48 (17) (2000) 4181–4189.
[17] N. Jia, P. Eisenlohr, F. Roters, D. Raabe, X. Zhao, Orientation dependence of shear banding in face-centered-cubic single crystals, Acta Mater. 60 (8) (2012) 3415–3434.
[18] N. Jia, F. Roters, P. Eisenlohr, C. Kords, D. Raabe, Non-crystallographic shear banding in crystal plasticity FEM simulations: example of texture evolution in α-brass, Acta Mater. 60 (3) (2012) 1099–1115.
[19] G.Y. Chin, W.F. Hosford, D.R. Mendorf, Accommodation of constrained deformation in f.c.c. metals by slip and twinning, Proceedings of the Royal Society of London A: Mathematical, Phys. Eng. Sci. 309 (1499) (1969) 433–456.
[20] G.I. Taylor, Plastic strain in metals, J. Inst. Metals 62 (1938) 307–324.
[21] P. Van Houtte, Simulation of the rolling and shear texture of brass by the Taylor theory adapted for mechanical twinning, Acta Metall. 26 (4) (1978) 591–604.
[22] C.N. Tomé, R.A. Lebensohn, U.F. Kocks, A model for texture development dominated by deformation twinning: application to zirconium alloys, Acta Metallurgica Materialia 39 (11) (1991) 2667–2680.
[23] R.A. Lebensohn, C.N. Tomé, A self-consistent viscoplastic model: prediction of rolling textures of anisotropic polycrystals, Mater. Sci. Eng. A 175 (1) (1994) 71–82.
[24] S.R. Kalidindi, Incorporation of deformation twinning in crystal plasticity models, J. Mech. Phys. Solids 46 (2) (1998) 267–290.
[25] A. Staroselsky, L. Anand, Inelastic deformation of polycrystalline face centered cubic materials by slip and twinning, J. Mech. Phys. Solids 46 (4) (1998) 671–696.
[26] S.R. Kalidindi, Modeling the strain hardening response of low SFE FCC alloys, Int. J. Plasticity 14 (12) (1998) 1265–1277.
[27] S.R. Kalidindi, Modeling anisotropic strain hardening and deformation textures in low stacking fault energy fcc metals, Int. J. Plasticity 17 (6) (2001) 837–860.
[28] L. Remy, Kinetics of f.c.c. deformation twinning and its relationship to stress-strain behaviour, Acta Metall. 26 (3) (1978) 443–451.
[29] I. Karaman, H. Sehitoglu, A.J. Beaudoin, Y.I. Chumlyakov, H.J. Maier, C.N. Tomé, Modeling the deformation behavior of Hadfield steel single and polycrystals due to twinning and slip, Acta Mater. 48 (9) (2000) 2031–2047.
[30] O. Bouaziz, N. Guelton, Modelling of TWIP effect on work-hardening, Mater. Sci. Eng. A 319–321 (2001) 246–249.
[31] S. Allain, J.-P. Chateau, O. Bouaziz, A physical model of the twinning-induced plasticity effect in a high manganese austenitic steel, Mater. Sci. Eng. A 387–389 (2004) 143–147.
[32] S. Allain, J.-P. Chateau, D. Dahmoun, O. Bouaziz, Modeling of mechanical

twinning in a high manganese content austenitic steel, Mater. Sci. Eng. A 387–389 (2004) 272–276.
[33] G.B. Olson, M. Cohen, Kinetics of strain-induced martensitic nucleation, Metall. Trans. A 6 (4) (1975) 791–795.
[34] R.G. Stringfellow, D.M. Parks, G.B. Olson, A constitutive model for transformation plasticity accompanying strain-induced martensitic transformations in metastable austenitic steels, Acta Metallurgica Materialia 40 (7) (1992) 1703–1716.
[35] J.B. Leblond, G. Mottet, J.C. Devaux, A theoretical and numerical approach to the plastic behaviour of steels during phase transformations—I. derivation general relation, J. Mech. Phys. Solids 34 (4) (1986) 395–409.
[36] J.B. Leblond, G. Mottet, J.C. Devaux, A theoretical and numerical approach to the plastic behaviour of steels during phase transformations—II. Study of classical plasticity for ideal-plastic phases, J. Mech. Phys. Solids 34 (4) (1986) 411–432.
[37] F. Marketz, F.D. Fischer, Micromechanical modelling of stress-assisted martensitic transformation, Model. Simul. Mater. Sci. Eng. 2 (5) (1994) 1017–1046.
[38] F. Marketz, F.D. Fischer, A mesoscale study on the thermodynamic effect of stress on martensitic transformation, Metallurgical Mater. Trans. A 26 (2) (1995) 267–278.
[39] Y. Tomita, T. Iwamoto, Constitutive modeling of TRIP steel and its application to the improvement of mechanical properties, Int. J. Mech. Sci. 37 (12) (1995) 1295–1305.
[40] J.M. Diani, H. Sabar, M. Berveiller, Micromechanical modelling of the transformation induced plasticity (TRIP) phenomenon in steels, Int. J. Eng. Sci. 33 (13) (1995) 1921–1934.
[41] J.M. Diani, D.M. Parks, Effects of strain state on the kinetics of strain-induced martensite in steels, J. Mech. Phys. Solids 46 (9) (1998) 1613–1635.
[42] M. Cherkaoui, M. Berveiller, H. Sabar, Micromechanical modeling of martensitic transformation induced plasticity (TRIP) in austenitic single crystals, Int. J. Plasticity 14 (7) (1998) 597–626.
[43] M. Cherkaoui, M. Berveiller, X. Lemoine, Couplings between plasticity and martensitic phase transformation: overall behavior of polycrystalline TRIP steels, Int. J. Plasticity 16 (10–11) (2000) 1215–1241.
[44] S. Turteltaub, A.S.J. Suiker, Transformation-induced plasticity in ferrous alloys, J. Mech. Phys. Solids 53 (8) (2005) 1747–1788.
[45] A.S.J. Suiker, S. Turteltaub, Computational modelling of plasticity induced by martensitic phase transformations, Int. J. Numer. Methods Eng. 63 (12) (2005) 1655–1693.
[46] S. Turteltaub, A.S.J. Suiker, A multiscale thermomechanical model for cubic to tetragonal martensitic phase transformations, Int. J. Solids Struct. 43 (14–15) (2006) 4509–4545.
[47] M.S. Wechsler, D.E. Lieberman, T.A. Read, On the theory of the formation of martensite, Trans. AIME 197 (1953) 1503–1515.
[48] J.M. Ball, R.D. James, Fine phase mixtures as minimizers of energy, Archive Ration. Mech. Analysis 100 (1) (1987) 13–52.
[49] C.Y. Sun, N. Guo, M.W. Fu, S.W. Wang, Modeling of slip, twinning and transformation induced plastic deformation for TWIP steel based on crystal plasticity, Int. J. Plasticity 76 (2016) 186–212.
[50] L.J. Teutonico, The dissociation of dislocations in the face-centered cubic structure, Acta Metall. 11 (12) (1963) 1283–1289.
[51] J.P. Hirth, J. Lothe, Theory of Dislocations, John Wiley & Sons, New York, 1982.
[52] J.W. Christian, S. Mahajan, Deformation twinning, Prog. Mater. Sci. 39 (1–2) (1995) 1–157.
[53] J.W. Christian, A theory of the transformation in pure cobalt, proceedings of the royal society of London a: mathematical, Phys. Eng. Sci. 206 (1084) (1951) 51–64.
[54] G.B. Olson, M. Cohen, A mechanism for the strain-induced nucleation of martensitic transformations, J. Less Common Metals 28 (1) (1972) 107–118.
[55] S. Mahajan, M.L. Green, D. Brasen, A model for the FCC → HCP transformation, its applications, and experimental evidence, Metall. Trans. A 8 (2) (1977) 283–293.
[56] F. Roters, Advanced Material Models for the Crystal Plasticity Finite Element Method – Development of a General CPFEM Framework, Habilitation thesis, 2011.
[57] E.H. Lee, Elastic-plastic deformation at finite strains, J. Appl. Mech. 36 (1) (1969) 1–6.
[58] Z. Nishiyama, Martensitic Transformation, Academic Press, 1978.
[59] E. Orowan, Zur Kristallplastizität. I–III, Z. für Phys. 89 (9–10) (1934) 605–613.
[60] R. Twardowski, Mikrostrukturelle Beschreibung von Verformung und Schädigung hochmanganhaltiger Stähle mit TRIP- und TWIP-Effekt, Ph.D. thesis, RWTH Aachen, 2013.
[61] E.O. Hall, Yield Point Phenomena in Metals and Alloys, Plenum Press, New York, 1970.
[62] T. Gebhardt, D. Music, B. Hallstedt, M. Ekholm, I.A. Abrikosov, L. Vitos, J.M. Schneider, Ab initio lattice stability of fcc and hcp Fe–Mn random alloys, J. Phys. Condens. Matter 22 (29) (2010) 295402.
[63] H.M. Rietveld, Line profiles of neutron powder-diffraction peaks for structure refinement, Acta Crystallogr. 22 (1) (1967) 151–152.
[64] H.M. Rietveld, A profile refinement method for nuclear and magnetic structures, J. Appl. Crystallogr. 2 (2) (1969) 65–71.
[65] H.C. Choi, T.K. Ha, H.C. Shin, Y.W. Chang, The formation kinetics of deformation twin and deformation induced ε-martensite in an austenitic Fe-C-Mn steel, Scr. Mater. 40 (10) (1999) 1171–1177.
[66] D. Music, T. Takahashi, L. Vitos, C. Asker, I.A. Abrikosov, J.M. Schneider, Elastic properties of Fe–Mn random alloys studied by ab initio calculations, Appl. Phys. Lett. 91 (2007) 191904.
[67] R.M. Martin, Relation between elastic tensors of wurtzite and zinc-blende structure materials, Phys. Rev. B 6 (1972) 4546–4553.
[68] E.R. Fuller, W.F. Weston, Relation between elastic–constant tensors of hexagonal and cubic structures, J. Appl. Phys. 45 (1974) 3772–3776.
[69] J.P. Hirth, Thermodynamics of stacking faults, Metall. Trans. 1 (9) (1970) 2367–2374.
[70] G.B. Olson, M. Cohen, A general mechanism of martensitic nucleation: Part I. General concepts and the FCC → HCP transformation, Metall. Trans. A 7 (12) (1976) 1897–1904.
[71] A. Saeed-Akbari, J. Imlau, U. Prahl, W. Bleck, Derivation and variation in composition-dependent stacking fault energy maps based on subregular solution model in high-manganese steels, Metallurgical Mater. Trans. A 40 (13) (2009) 3076–3090.
[72] A. Dumay, J.-P. Chateau, S. Allain, S. Migot, O. Bouaziz, Influence of addition elements on the stacking-fault energy and mechanical properties of an austenitic Fe–Mn–C steel, Mater. Sci. Eng. A 483–484 (2008), 184–187, 14th International Conference on the Strength of Materials.
[73] D.P. Escobar, S.S.F. de Dafé, D.B. Santos, Martensite reversion and texture formation in 17Mn-0.06C TRIP/TWIP steel after hot cold rolling and annealing, J. Mater. Res. Technol. 4 (2) (2015) 162–170.
[74] L. Vitos, J.-O. Nilsson, B. Johansson, Alloying effects on the stacking fault energy in austenitic stainless steels from first-principles theory, Acta Mater. 54 (14) (2006) 3821–3826.
[75] A. Dick, T. Hickel, J. Neugebauer, The effect of disorder on the concentration-dependence of stacking fault energies in Fe_{1-x} Mnx – a first principles study, Steel Res. Int. 80 (9) (2009) 603–608.
[76] A. Asghari, A. Zarei-Hanzaki, M. Eskandari, Temperature dependence of plastic deformation mechanisms in a modified transformation-twinning induced plasticity steel, Mater. Sci. Eng. A 579 (2013) 150–156.
[77] J.-K. Kim, L. Chen, H.-S. Kim, S.-K. Kim, Y. Estrin, B.C. Cooman, On the tensile behavior of high-manganese twinning-induced plasticity steel, Metallurgical Mater. Trans. A 40 (13) (2009) 3147–3158.
[78] P.D. Zavattieri, V. Savic, L.G. H. Jr, J.R. Fekete, W. Tong, Y. Xuan, Spatio-temporal characteristics of the Portevin–Le Châtelier effect in austenitic steel with twinning induced plasticity, Int. J. Plasticity 25 (12) (2009) 2298–2330.
[79] O. Bouaziz, S. Allain, C. Scott, P. Cugy, D. Barbier, High manganese austenitic twinning induced plasticity steels: a review of the microstructure properties relationships, Curr. Opin. Solid State Mater. Sci. 15 (4) (2011) 141–168.
[80] W.F. Hosford, Mechanical Behavior of Materials, Cambridge University Press, 2005.